

Identification of different silicon vacancy centers in 6H-SiC

Harpreet Singh¹, Andrei N. Anisimov^{1,2}, Pavel G. Baranov² and Dieter Suter¹

¹Fakultät Physik, Technische Universität Dortmund,

D-44221 Dortmund, Germany. ²Ioffe Institute, St. Petersburg 194021, Russia.

Silicon vacancies in silicon carbide (SiC) have been proposed as interesting candidates for quantum technology applications such as quantum sensing and quantum repeaters. SiC exists in many polytypes with different plane stacking sequences, and in each polytype, the vacancies can occupy a variety of different lattice sites. In this work, we characterize and identify the three most important charged silicon vacancies in the 6H-SiC polytype. We record the photoluminescence and continuous-wave optically detected magnetic resonance spectra at different radio-frequency power levels and different temperatures. We individually select the zero-phonon lines of the different silicon vacancies at low temperatures and record the corresponding optically detected magnetic resonance (ODMR) spectra. ODMR allows us to correlate optical and magnetic resonance spectra and thereby resolve a controversy from earlier work.

I. INTRODUCTION

Silicon carbide (SiC) is an interesting material for a range of applications that rely on its wide bandgap and established manufacturing processes [1–6]. It contains different types of silicon vacancies, carbon vacancies and silicon-carbon divacancies, which show remarkable spin properties that make them promising candidates for new quantum technologies. Silicon vacancies, as a specific example, are negatively charged and have spin 3/2 [7]. Irradiation with visible or near-infrared light results in nonthermal population of the spin states. Two characteristic parameters of V_{Si}^- centers are the emission wavelength and the zero field splitting.

In the low temperature photoluminescence (PL) spectra, different centers can be identified by their emission wavelengths. In sequence of increasing wavelengths, they are therefore labeled V_1 , V_2 and V_3 . In terms of the local structure, they are associated with different lattice sites where the environment has cubic (k) or hexagonal (h) symmetry. The correspondence between emission wavelength and lattice sites is a matter of ongoing controversy [8–12].

In an earlier paper, we characterized silicon vacancies in 6H-SiC [13] in terms of their photoemission as well as their spin Hamiltonian, using optically detected magnetic resonance (ODMR). Since ODMR correlates optical properties with energy differences between spin states, it provides a useful approach for associating the zero-field splittings with the emission wavelengths. The goal of this work is to identify the different types of V_{Si}^- centers in 6H-SiC. For this purpose, we combine photoluminescence (PL) measurements at different wavelengths and different polarizations with radio-frequency excitation of the spin transitions to record ODMR spectra under a range of different conditions, including its temperature dependence.

This work is structured as follows: Section II introduces the spin system of the sample, as well as its photoluminescence as a function of the direction and orientation of the emission, and separates it into the contributions of the

3 types of vacancies. Section III shows the temperature-dependent ODMR spectra for emission parallel and perpendicular to the c -axis. To distinguish the contributions from the different types of centers, we record signals at different wavelengths separately. Section IV contains the spin-lattice and spin-spin relaxation times obtained by time-resolved ODMR. Section V contains a brief discussion and concluding remarks.

II. SYSTEM

For creating silicon vacancies homogeneously, the sample can be irradiated with neutrons or electrons [14, 15]. Neutron irradiation leads to more lattice damage than electron irradiation and creates many other unwanted defects, resulting in faster relaxation rates of the vacancy spins [16]. For this work, we therefore used electron irradiation of a 6H-SiC sample [17]. More details of the sample preparation are given in Appendix A.

At the silicon vacancy site, four dangling sp^3 orbitals contribute four electrons. In addition, the silicon vacancy can capture one or two electrons, depending on the Fermi level, and become a negatively charged silicon vacancy (V_{Si}^-). Here, we only consider centers with a single negative charge, which have a spin of 3/2 [7]. The energy levels of these vacancies can be determined from a PL spectrum.

A. Photoluminescence

We start the characterisation of the sample with the photoluminescence spectra. Depending on the transition dipole, whose orientation varies with the different types of vacancies [13, 18], the PL emission shows an orientation dependence. We therefore recorded PL spectra for emission parallel and perpendicular to the c -axis. The detailed description of the PL setup is given in Appendix B. Figures 1 (a) and (b) show the PL spectra recorded for emission parallel and perpendicular to the c -axis at 5 K.

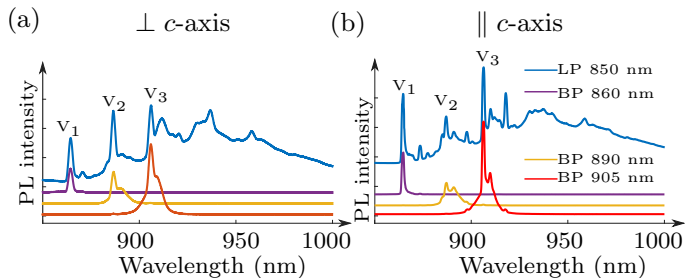


FIG. 1. Photoluminescence (PL) recorded with different optical filters at 5K (a) for photons emitted \perp to the c -axis and (b) \parallel to the c -axis. PL spectra obtained by filtering the PL with 860 nm, 890 nm and 905 nm bandpass filters of 10 nm bandwidth to select the zero-phonon line of V_1 , V_2 , and V_3 type V_{Si}^- .

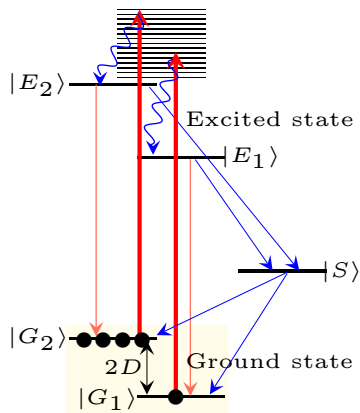


FIG. 2. Energy level diagram of V_{Si}^- and optical pumping scheme. $|G_i\rangle$ are the spin states of the electronic ground state $|E_i\rangle$, correspond to the electronically excited state and $|S\rangle$ is the shelving state.

In addition to the full spectra, where we used an 850 nm long-pass (LP) filter to suppress scattered laser light, we also recorded spectra with 860 nm, 890 nm and 905 nm bandpass (BP) filters. The zero phonon lines (ZPL) of the different V_{Si}^- are clearly visible in the spectra at 865 nm (V_1), 887 nm (V_2), and 908 nm (V_3) [8, 10]. Comparison of the two sets of spectra shows that V_1 and V_3 emit more PL parallel to the c -axis, while V_2 emits more perpendicular to the c -axis [13, 19, 20].

The assignment of the emission lines to specific lattice sites was debated in the literature. An early study of 6H-SiC [10], indicated that V_1 and V_3 correspond to V_{Si}^- at the cubic lattice sites k_1 and k_2 and V_2 corresponds to the hexagonal lattice site h . However, more detailed

studies indicate that V_1 corresponds to the hexagonal lattice site h and V_2 and V_3 to the cubic lattice sites k_2 and k_1 respectively [11, 12]. We adopt the latter assignment here.

B. Spin

We consider the $S = 3/2$ spin of a V_{Si}^- center in the absence of an external magnetic field. Figure 2 shows the relevant part of the energy level diagram. The states $|G_1\rangle$ and $|G_2\rangle$ are doubly degenerate spin substates of the electronic ground state with $m_s = \pm 1/2$ and $\pm 3/2$ in the case of V_1 and V_2 [8, 12]. In the case of V_3 , the zero field splitting is negative and the lowest energy state is therefore $m_s = \pm 3/2$ [12, 21]. Similarly, the states $|E_1\rangle$ and $|E_2\rangle$ are spin states of the electronically excited state. The state $|S\rangle$ represents the shelving state, which has spin $S=1/2$ and plays an essential role for generating spin polarization by optical pumping [8, 22]. Laser illumination excites transitions from the ground states $|G_1\rangle$ and $|G_2\rangle$ to the excited states $|E_1\rangle$ and $|E_2\rangle$. From the excited states $|E_i\rangle$, most of the population falls back to the ground states $|G_i\rangle$ due to spontaneous emission. A smaller fraction undergoes intersystem crossing (ISC) to the shelving state $|S\rangle$, and from there, preferentially populates the ground state $|G_2\rangle$, as shown in Fig. 2.

In the absence of an external magnetic field, the effective spin Hamiltonian is

$$\mathcal{H} = D(S_z^2 - 5/4), \quad (1)$$

where D is the zero-field splitting constant whose value depends on environment of the center. S_z is the electron spin operator along the z axis ($\parallel c$ axis). In the magnetic resonance spectra, we therefore expect a single resonance line at frequency $2D$ for every type of vacancy. Figure 3 shows, as an example, an ODMR spectrum of a 6H-SiC sample that contains three different types of vacancies. It consists of two resonance lines close to 28 MHz and 130 MHz. The assignment of these resonance lines to the different types of V_{Si}^- in 6H-SiC has been somewhat contentious, in particular with respect to V_1 . Table I provides a summary of data. While Davidsson *et al.* [12] assume that V_1 contributes to the resonance near 28 MHz, Biktagirotov *et al.* [11] suggest that it is close to zero and therefore not observable. In the following section, we attempt to resolve this issue by measuring ODMR spectra at low temperatures and separating the PL from the ZPLs of the 3 different vacancies using suitable optical bandpass filters.

III. OPTICALLY DETECTED MAGNETIC RESONANCE

Optically detected magnetic resonance (ODMR) combines optical measurements with electron spin resonance

spectroscopy. Compared to conventional EPR, this double resonance technique increases the sensitivity and information content of magnetic resonance [24, 25]. For

V_{si}^-	Temp	$S_{max}(\Delta PL/PL)$	P_0 (W)	LW_0 (MHz)	a (MHz W ^{-1/2})
V_1/V_3	5 K	-0.014 ± 0.001	0.023 ± 0.012	5.5 ± 0.8	2.3 ± 0.7
V_2	298 K	-0.069 ± 0.007	0.070 ± 0.043	8.4 ± 0.7	3.7 ± 0.6
V_2	5K	-0.234 ± 0.054	0.097 ± 0.097	7.5 ± 0.4	3.4 ± 0.4
V_1/V_3	298 K	0.14 ± 0.01	0.05 ± 0.03	6.6 ± 0.4	3.4 ± 0.3

TABLE II. Fitting parameters of Eqs (2) and (3).

Center	Sorman <i>et al.</i> [10]	Davidsson <i>et al.</i> [12]	Biktagirov <i>et al.</i> [11]	Astakhov <i>et al.</i> [23]
	Exp	Exp	Exp	Exp
	$2D^g$ (Site)	$2D^g$ (Site)	$ 2D^g $ (Site)	$ 2D^e $ (MHz)
V_1	27.6 MHz (k_1)	26.6 MHz (h)	0 (h)	367
V_2	128.4 MHz (h)	128 MHz (k_2)	128 MHz (k_2)	1030
V_3	27.6 MHz (k_2)	27.8 MHz (k_1)	28 MHz (k_1)	367

TABLE I. Experimental values for the zero field splittings (ZFS) splittings $2D$ for the 3 types of different V_{si}^- in 6H-SiC. The upper indices g and e refer to the electronic ground and excited states. The values and the proposed assignments to the different types of centers are taken from 4 earlier publications.

low-temperature ODMR, we placed the sample in a liquid helium flow cryostat and irradiated it with 785 nm laser light. The emitted PL was collected using a convex lens and focused with another convex lens on an avalanche photodiode (APD) via a suitable optical filter. The photocurrent was measured with a lock-in amplifier. A radio-frequency (RF) field was applied to the sample through a wire (for continuous-Wave ODMR) or a coil (for pulsed experiments), terminated with a 50-Ohm resistor. To reduce background signal, we modulated the RF with a TTL signal from a digital word generator (DWG) and demodulated the APD signal with a lock-in amplifier referenced to the TTL signal. Appendix B provides a detailed description of the ODMR setup.

A. Dependence on RF Power

Figure 3 (a) shows ODMR spectra recorded with different RF powers at room temperature (296 K) and at 5 K. These spectra were recorded with a 850 nm long pass optical filter, which suppresses the scattered laser light but passes most of the PL from V_{si}^- . At low RF power,

only two ODMR peaks are visible near 28 MHz and 130 MHz. With increasing RF power, additional resonances appear at 14 MHz (P_3^2), 42 MHz (P_2^3), and 64 MHz (P_2^2). The peak P_3^2 is due to the absorption of 2 RF photons by the V_1/V_3 vacancy [17], whereas the peaks P_2^2 and P_2^3 are due to 2 and 3 photon absorption by the V_2 vacancy [17]. Figure 3 (b) shows the amplitudes of the 1-photon peaks of V_1/V_3 and V_2 vs. the applied RF power: they increase with the applied power but saturate for $P > 0.3$ W. This behaviour can be fitted with the function

$$S(P) = S_{max}[P/(P_0 + P)], \quad (2)$$

where $S(P)$ is the signal amplitude at power P , S_{max} is the asymptotic amplitude and P_0 the saturation power. The resulting fitting parameters are given in Table II. Figure 3 (c) shows the linewidths of the 1-photon peaks of V_1/V_3 and V_2 vs. the RF power. The linewidth data $LW(P)$ were fitted to the function

$$LW(P) = LW_0 + a\sqrt{P}, \quad (3)$$

where LW_0 and a are the fitting parameters and their values are given in Table II.

B. Temperature dependence

Figures 4 (a) and (b) show the ODMR spectra for the range of temperatures from 5 K to 290 K when the PL is recorded parallel and perpendicular to the c -axis using an RF power of 26 dBm (0.3 W). The horizontal axis corresponds to the RF frequency, and the vertical axis to the temperature. The color represents the relative change of PL, as indicated by the scale bar on the right. The ODMR signal near 130 MHz, which corresponds to V_2 , increases with decreasing temperature while the ODMR

signal near 28 MHz, which is due to V_1/V_3 , decreases. We recorded larger ODMR signals ($\Delta PL/PL$) when the PL is emitted parallel to the c -axis in the case of V_1/V_3 , whereas the ODMR signal of V_2 was larger for emission $\perp c$. In both orientations, the V_2 signal increases with decreasing temperature, while it gets smaller in the case of V_1/V_3 . However, for PL emitted parallel to the c -axis, the ODMR signal near 28 MHz changes sign. Figure 4 (c), shows that the ODMR signal vanishes at 22 K and becomes negative at 15 K. At even lower temperatures, the negative signal increases in magnitude.

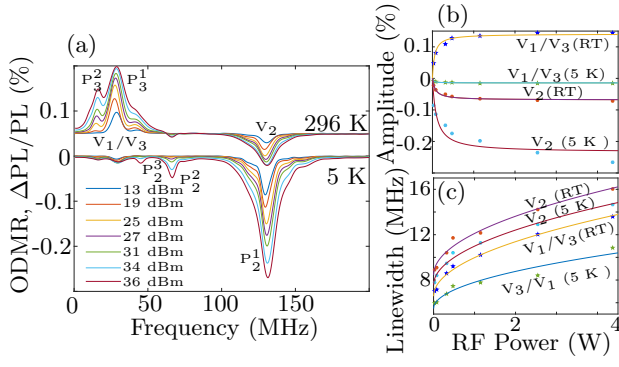


FIG. 3. (a) ODMR signal vs. frequency recorded with different RF powers in zero magnetic field at 5 K and 296 K. The horizontal axis is the frequency in MHz and the vertical axis the relative change of the PL, recorded by the lock-in amplifier. (b) ODMR signal vs RF power and (c) linewidth vs RF power.

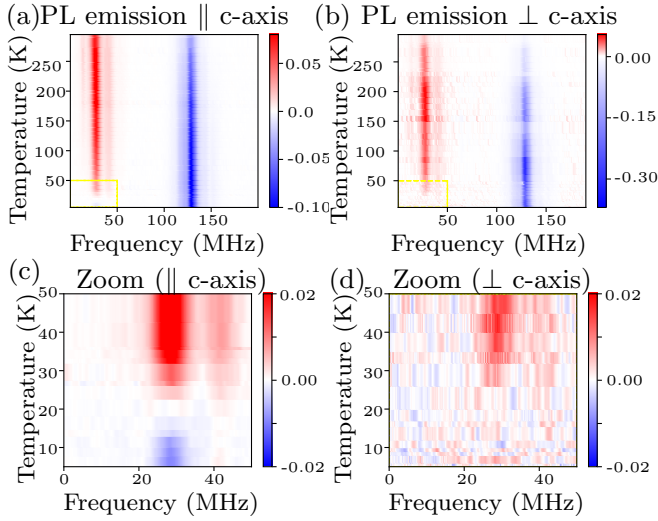


FIG. 4. ODMR signal as a function of temperature recorded with PL emitted (a, c) parallel and (b, d) perpendicular to the c -axis. The range from 5 MHz to 50 MHz is shown on an expanded scale in (c, d). The color scale and the y -axis of the 1D spectra are in units of $\Delta\text{PL}/\text{PL}\%$.

Figures 6 (a) and (b) show the measured frequency of the ODMR resonance lines that correspond to the ZFS as a function of temperature. (a) corresponds to the V_2 center while the resonance line near 28 MHz is dominated by the signal from V_3 in the temperature range from 36 K to 295 K. The extracted data is fitted to the function

$$\text{ZFS}(T) = \text{ZFS}_0 + bT^2. \quad (4)$$

The best fits are obtained for the parameters $\text{ZFS}_0 = 129.9 \pm 0.5$ MHz and 28.64 ± 0.02 MHz, $b = (-1.19 \pm 0.02) \times 10^{-5}$ MHz K^{-2} and $(-1.52 \pm 0.02) \times 10^{-5}$ MHz K^{-2} for V_2 and V_1/V_3 , respectively. These results correspond to an improvement over earlier reports that

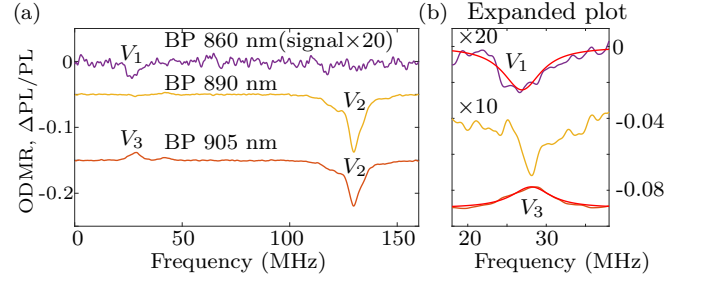


FIG. 5. (a) ODMR spectra recorded with different optical filters at 28 K for PL emitted parallel to the c -axis. 860 nm, 890 nm and 905 nm bandpass filters were used to select the zero-phonon lines of V_1 , V_2 , and V_3 . (b) The range from 18 MHz to 38 MHz, where the V_1 and V_3 resonances are located, are shown on an expanded scale. The main peaks were fitted to a Lorentzian. With the 860 nm and 905 nm BP filters, the center frequencies are 27 MHz and 28.08 MHz, respectively.

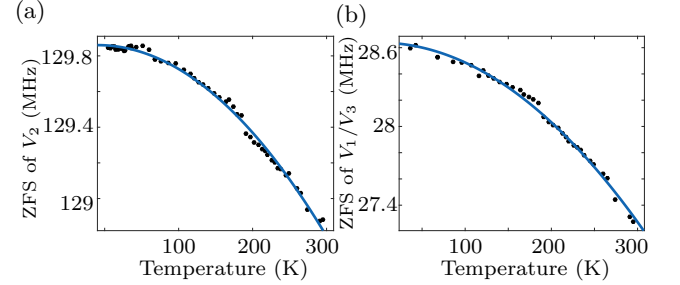


FIG. 6. Measured temperature dependence of the ZFS of the resonance lines near 130 (a) and 28 MHz (b).

the ground-state ZFS does not depend on temperature [23].

C. Optically selective detection

For a better identification of the different ODMR signals, we only collect PL from specific wavelength ranges by passing it through different optical filters. Figure 5 (a) shows the ODMR spectra recorded with different bandpass (BP) filters at 28 K for PL emitted $\parallel c$ -axis. The top, middle, and bottom spectra were recorded with 860 nm, 890 nm, and 905 nm BP (10 nm bandwidth) filters, which predominantly select PL from the zero-phonon line (ZPL) of the V_1 , V_2 , and V_3 vacancies, respectively.

The top spectrum (860 nm BP), contains only a small negative peak at 27 ± 1 MHz. This differs strongly from the ODMR spectra in Fig. 3 recorded with the 850 nm LP filter, where we observed two single-photon resonances near 28 MHz and 130 MHz. Since the 860 nm BP filter selects the ZPL of V_1 , we assign the negative peak at 27 MHz to V_1 . Since the signal is quite small under these conditions, we expanded the vertical scale of the top spectrum by a factor of 20 to make the peak visible.

The middle ODMR spectrum was recorded with a BP filter centered at the ZPL of V_2 . It is dominated by a signal at 130 ± 0.01 MHz, which we therefore attribute to V_2 . The bottom ODMR spectrum was recorded with the 905 nm BP filter; we observe one negative and two positive peaks. We attribute the positive peak at 28.1 ± 0.6 MHz to the V_3 center, whose ZPL coincides with the center of the 905 nm BP filter. The negative peak at 129.93 ± 0.03 MHz is due to the phonon sidebands (PSB) of V_2 , which extend well into the range of the 905 BP filter.

Figure 5 (b) shows the frequency range from 18 MHz to 38 MHz, where the signals from V_1 and V_3 are centered, on an expanded scale. In the top spectrum, the signal from V_1 dominates, in the bottom spectrum that from V_3 .

As an additional way to distinguish between the PL emitted by V_1 and V_3 , we also measured ODMR spectra with polarizers at different orientations. The corresponding data are presented in appendices E and F.

D. Separating the contributions from V_1 and V_3

As discussed in the introduction, there is conflicting evidence on the ZFS of V_1 and V_3 . The experiments presented in subsections IIIB and IIIC were designed to provide data for distinguishing between them. The results can be interpreted consistently if we assume that the ZFS splittings of V_1 and V_3 are both close to 28 MHz but have slightly different frequencies (27 MHz and 28 MHz) and contribute to the ODMR spectrum with opposite signs: for V_1 , the ODMR signal is negative ($\Delta PL/PL < 0$), for V_3 it is positive. Since the combined linewidth is larger than the separation between the two resonance frequencies, only a single line is observed and the two signals partially cancel. Since the PL from the two centers show different polarisation, the positive and negative signal contribution depend differently on the orientation of the polarizer, as shown in Appendix F.

The signals from the two centers also have different temperature dependence. At low temperatures, the V_1 signal at 27 MHz dominates, resulting in an overall negative signal but at high temperatures, the V_3 signal at 28 MHz dominates, resulting in an overall positive signal. For a more detailed analysis, we compare the experimental signal at different temperatures to a theoretical spectrum consisting of two Lorentzians with the frequencies of V_1 and V_3 and opposite amplitudes

$$S(f, T) = \frac{A_1(T) \sigma_1}{(f - ZFS_1)^2 + \sigma_1^2} + \frac{A_3(T) \sigma_3}{(f - ZFS_3)^2 + \sigma_3^2}. \quad (5)$$

The frequencies $ZFS_{i=1,3} = 2D$ were calculated from Eq. (4) for different temperatures, using the temperature coefficient $b = (-1.52 \pm 0.02) \times 10^{-5}$ MHz K $^{-2}$ for V_1 and V_3 . The values of the ZFS at $T = 0$ were determined from the spectra measured with optical filters at

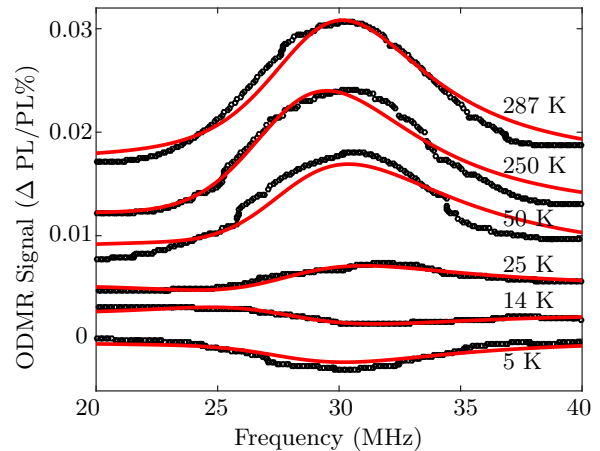


FIG. 7. ODMR spectra measured with the 850 nm LP filter at different temperatures for PL emitted parallel to the c -axis. Only the region of the V_1 and V_3 resonances is shown and the spectra are fitted to a sum of two Lorentzians.

28 K as $ZFS_0 = 26.99$ MHz and 27.99 MHz for V_1 and V_3 . The linewidths $\sigma_1 = 5.9$ MHz and $\sigma_3 = 6.1$ MHz were also taken from the spectra measured at 28 K.

Figure 7 shows the ODMR spectra for the frequency range 10 to 50 MHz at different temperatures, together with a fitted signal, where only the amplitudes A_i were taken as fitting parameters to measure the contributions from V_1 and V_3 . Overall, the superposition of the two resonance lines yields excellent agreement with the experimental data.

For PL emitted $\perp c$, the signal near 28 MHz decreases with temperature but does not become negative, as shown in Fig. 4 (d). This is also consistent with the assumption that the negative signal is associated with V_1 : as shown in appendix E, V_1 emits less PL perpendicular to the c -axis as shown in Fig.1 and therefore can not dominate over the contribution from V_3 .

IV. RELAXATION MEASUREMENTS

In this section we focus on the evolution of the spin system towards thermal equilibrium, which is driven by interactions with the environment [26]. Each type of silicon vacancies has a different structure and therefore different interactions with the environment that can be probed by relaxation measurements.

A. Population relaxation

The spin-lattice interaction drives the spin system towards thermal equilibrium with its environment. Under our experimental conditions, the thermal equilibrium spin state is completely unpolarised, i.e. the density op-

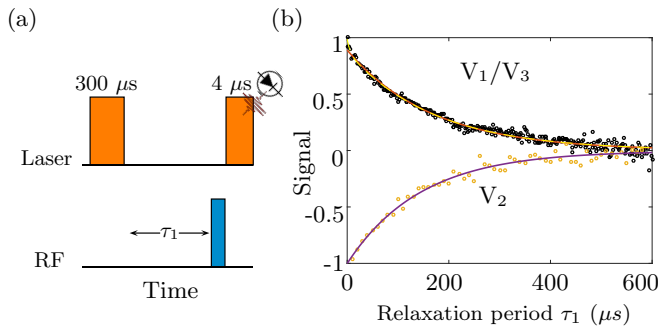


FIG. 8. (a) Pulse sequence used to measure the T_1 relaxation. The orange and blue rectangles represent the laser and RF pulses. The duration of the laser pulses is written above each pulse. (b) Resulting signal (normalized) as a function of the delay τ_1 , measured at room temperature. The experimental data (circles) for V_2 and V_1/V_3 are fitted to function Eq.6.

erator is proportional to the unit operator. The time scale on which the system approaches this equilibrium state is characterized by the spin-lattice relaxation time T_1 . Figure 8(a) shows the pulse sequence used to measure the T_1 relaxation time. A $300 \mu\text{s}$ laser pulse was applied to polarize the spin system, which was then allowed to evolve for a time τ_1 . An RF pulse with flip angle π was applied before measuring the remaining spin polarisation with a second laser pulse of $4 \mu\text{s}$. The measured signal was subtracted from the reference signal obtained without applying the RF pulse[17, 20, 22]. Figure 8(b) shows the measured signal vs. the delay τ_1 . The recorded experimental data can be fitted by an exponential

$$S_\pi(\tau_1) - S_0(\tau_1) = A e^{-\tau_1/T_1}. \quad (6)$$

At room temperature, the extracted relaxation times T_1 were $145 \pm 2 \mu\text{s}$ for V_2 and $166 \pm 2 \mu\text{s}$ for V_1/V_3 .

B. Dephasing

Relaxation affects not only the populations, but also the coherence of the spins. While population relaxation is dominated by fluctuations at the Larmor frequency, coherence dephases under the influence of (quasi-) static interactions. A free induction decay (FID) for both V_{Si}^- was measured using the Ramsey scheme [27]. The dephasing time T_2^* was $42 \pm 4 \text{ ns}$ for V_2 and $65 \pm 5 \text{ ns}$ for V_1/V_3 [17]. Details of the pulse sequence used and experimental data obtained are given in Appendix D. Next, we focus on homogeneous dephasing, which can be measured using the spin-echo experiment [28]. We refer to the time constant of the spin-echo decay as T_2 . Figure 9 (a) shows the pulse sequence. The system was again polarised with a $300 \mu\text{s}$ laser pulse. The first RF pulse with flip-angle $\pi/2$ generated coherence between the states $\pm 3/2 \leftrightarrow \pm 1/2$. The inhomogeneous dephas-

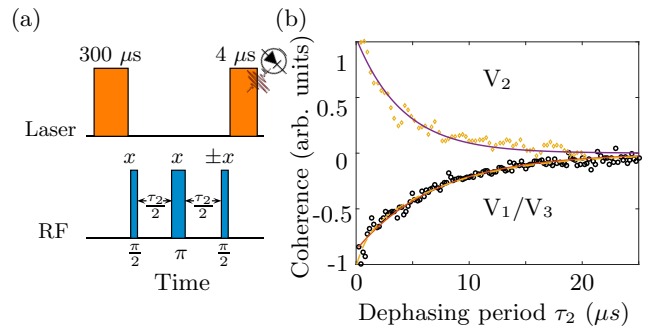


FIG. 9. (a) Pulse sequence for measuring the spin coherence time with a refocusing pulse. The red and blue rectangles represent the laser and RF pulses, respectively. (b) Decay of the spin coherence during the echo sequence. The experimental data (circles) for V_2 and V_1/V_3 are fitted to exponential functions.

Exp	^{13}C (1.1%) & ^{29}Si (4.7%)		^{13}C (4.7%) & ^{29}Si (0.1%) [20]	
	V_1/V_3	V_2	V_1/V_3	V_2
T_1	$166 \mu\text{s}$	$142 \mu\text{s}$	$142 \mu\text{s}$	$107 \mu\text{s}$
T_2^*	65 ns	42 ns	38 ns	31 ns
T_2^{SE}	$7.1 \mu\text{s}$	$4.6 \mu\text{s}$	$3.7 \mu\text{s}$	$3.3 \mu\text{s}$
T_2^{CPMG}	$57 \mu\text{s}$	$47 \mu\text{s}$	$56 \mu\text{s}$	$51 \mu\text{s}$

TABLE III. Comparison of room-temperature relaxation times of two 6H-SiC samples.

ing was reversed with a π pulse, which generated a spin-echo at time τ_2 after the initial $\pi/2$ pulse. A second $\pi/2$ RF pulse at the time of the echo converted the remaining coherence into population difference, which was measured by the final laser pulse [20, 22]. Figure 9(b) shows the experimental signal vs. the delay τ_2 . The recorded experimental data can again be fitted to a single exponential and the extracted dephasing times T_2 were $4.1 \pm 0.4 \mu\text{s}$ and $7.1 \pm 1.7 \mu\text{s}$ for V_2 and V_1/V_3 , respectively, roughly 2 orders of magnitude longer than T_2^* . The spin-echo data for V_1/V_3 does not fit well to the single exponential, so we also compared it to a sum of 2 exponentials ($A e^{-\tau_2/T_2^s} + B e^{-\tau_2/T_2^f}$), as shown in Fig. 9 with a yellow dashed curve ($A = -0.8 \pm 0.1$, $T_2^s = 7.7 \pm 0.3 \mu\text{s}$, $B = -0.2 \pm 0.1$, and $T_2^f = 0.8 \pm 0.4 \mu\text{s}$).

Next, we applied multiple refocusing pulses to further extend the coherence lifetime. These refocusing pulses remove the dephasing effect of non-static perturbations that have longer correlation times than the spacing between the refocusing pulses. The measured dephasing time T_2^{CPMG} for the V_2 (V_1/V_3) type of V_{Si}^- spin ensemble was $47 \pm 7 \mu\text{s}$ ($59 \pm 3 \mu\text{s}$) when the spacing between the refocusing pulses was 200 ns (100 ns), and the duration of each π pulse was 38 ns (40 ns). Details of the pulse sequence used and plots of the experimental data are given in Appendix D.

Table III, shows the comparison of the relaxation times measured in our previous paper where the 6H-SiC sample contained a higher concentration of ^{13}C but lower

concentration of ^{29}Si [20]. In the present sample, T_1 is slightly longer than in the sample used in [20], which indicates a somewhat lower concentration of paramagnetic centers [29]. The longer dephasing times T_2^* , T_2 can be attributed to the lower concentration of ^{13}C , which represent the nearest neighbors (NN) of the silicon vacancy. The higher concentration of ^{29}Si does not have a significant effect, since the silicon atoms have a much weaker hyperfine interaction.

V. DISCUSSION AND CONCLUSION

The V_{Si}^- center in SiC has attracted considerable interest in the context of emerging quantum technologies, since its spin can be optically polarized, has a sufficiently long coherence time and can be coherently controlled. These properties make it an attractive candidate for quantum information and quantum sensing. To develop this potential, it is essential to more precisely characterise its properties. They depend, e.g., on the lattice site at which the vacancy is created. In the $6H$ -SiC polytype, three different lattice sites exist, and the corresponding vacancies are referred to as V_1 , V_2 and V_3 .

In this work, we have gathered new data on all three types of vacancies. In particular, we related the properties of the PL of each center to the magnetic resonance by performing ODMR experiments for different optical frequencies, different optical polarizations and different directions of PL emission (parallel and perpendicular to the c -axis of the sample). We found that the V_1 and V_3 vacancies emit more PL parallel to the c -axis, whereas V_2 emits more perpendicular to the c -axis. ODMR experiments detecting photons that are emitted mostly by one type of center allowed us to determine the zero-field splitting of the V_1 vacancy, for which different values had been reported in previous works [11, 12]. Our results agree with those of Ref: [12]. With the identification of the ODMR frequencies of all three vacancies, we can explain the temperature dependence and change of sign of the ODMR signal near 28 MHz: At the high temperature, the signal from V_3 dominates but at low temperature the signal from V_1 dominates, which is negative. In real systems, the ZFS typically shows a small temperature variation. We checked the ZFS variation with temperature and found that the values increase by about 1 MHz as the temperature decreases from room temperature to 5 K.

Further, we measured the transverse and longitudinal relaxation rates. The relaxation rates measured here were lower than those reported earlier in a different sample [20] that contained a higher concentration of ^{13}C . In the spin-echo decay for V_1/V_3 , does not fit well to a single exponential, which may indicate differences in the relaxation of V_1 and V_3 . In future work, we will try to obtain more specific data for the relaxation times of the different centers and determine the different hyperfine coupling constants.

APPENDIX A: SAMPLE

Synthesized SiC crystals were grown with a low content of background impurities. We synthesized polycrystalline sources from semiconductor silicon and spectrally pure carbon. Spectrally pure graphite in powder form and polycrystalline silicon was chosen as sources. They were degassed using a resistive heating growth machine over 2 hours at 2200° C and 10^{-3} Torr under vacuum to prepare the crucible and internal furnace reinforcement for synthesis. After that, a stoichiometric mixture of carbon and silicon powders was loaded into the crucible. Manufacturing silicon carbide powder took place in a vacuum. Graphite with a minimum of background impurities was used to make the crucible, such as Mersen 6516PT. It should note that all parts of the crucible should be made from the same graphite. To avoid the destruction of parts, when the crucible is heated above the synthesis temperature of the source (above 1600°C). We used silicon carbide crystals polytype $6H$ as seeds. To grow crystals, the following conditions were used: 2050 ° C, 1 to 5 Torr argon pressure, 99.9999% pure argon, a growth rate of 150 μm / h. Crystals that grew under these conditions had no micropores more than 3 cm^{-2} .

APPENDIX B: PL SETUP

For measuring the photoluminescence (PL) at different temperature, the sample was cooled down using a helium cryostat. A tunable (799-813 nm) single-mode diode laser DL pro from Toptica Photonics modulated by a chopper was used to excite the sample optically. With the help of two convex lenses, PL was collected parallel to the c -axis of sample. The collected PL passed through a monochromator (Spex 1704) via an 850 nm long-pass filter (Thorlabs). For detecting the PL, an avalanche photodiode (APD) module with a frequency bandwidth from dc to 100 kHz (C5460-1 series from Hamamatsu) was attached to the monochromator. The output voltage of the APD was measured with the lock-in amplifier. The sync signal from the chopper was used as a reference for the lock-in amplifier [20].

APPENDIX C: ODMR SETUP

Figure 10 shows the setup used for the cw- and time-resolved ODMR measurements. For cooling the sample, we used a liquid helium flow cryostat (MicrostatHe-R from Oxford instruments). We used a turbopump for creating a vacuum in the cryostat pressure less than 10^{-6} mbar (from Pfeiffer vacuum). An LD785-SE400 diode laser was used as the light source (a laser diode controller (LDC202C series) and temperature controller (TED 200C). The laser light pulses were generated by an acoustic-optical modulator (NEC model OD8813A). We used three orthogonal coil pairs to apply a static

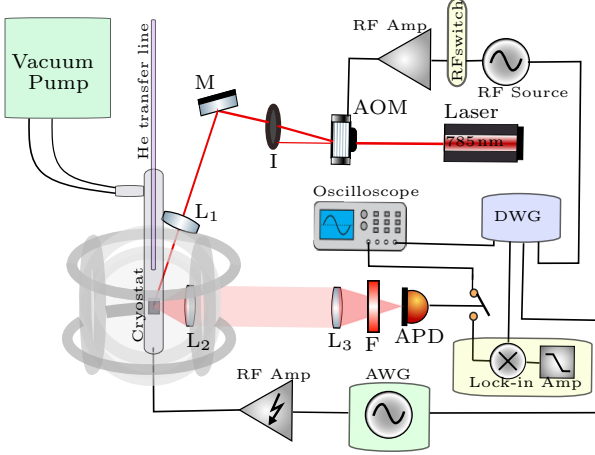


FIG. 10. Experimental setup for measuring ODMR at low temp.

magnetic field to the sample. APD module (C12703 series from Hamamatsu) was used to record the PL signal. APD signal was recorded with the PicoScope 2000 series USB oscilloscope card during pulse mode ODMR experiments. For cw-ODMR, the signal from APD was recorded with the lock-in (SRS model SR830 DSP). Analog Devices' AD9915 direct digital synthesizer (DDS) was used as an RF source for cw-ODMR experiments. We used a Hunter Micro DAX14000 arbitrary wave generator (AWG) for pulsed ODMR experiments. An RF signal from the source was amplified with an RF amplifier (LZY-22+ from mini circuits). For feeding RF power to a sample, we used wire and coil terminated with a 50-ohm resistor for continuous-wave and pulsed ODMR experiments, respectively. We generated TTL (transistor transistor logic) pulses using a digital word generator (DWG; SpinCore PulseBlaster ESR-PRO PCI card) to trigger the laser RF pulses.

APPENDIX D: ZFS WITH TEMPERATURE

APPENDIX D: FID AND CPMG

Figure. 11 (a) shows the pulse sequence for the FID measurement. A laser pulse of $300 \mu\text{s}$ and a power of 100 mW was used to polarize the vacancy spin ensemble. A delay τ_f was given between the two $\pi/2$ RF pulses, and the PL signal was using the second laser pulse. The phase of the first $\pi/2$ pulse was along x . For the second $\pi/2$ pulse, it was along $x + \phi_d$. We repeated the same sequence for the reference scan except for the phase of the second $\pi/2$ pulse was $-x + \phi_d$. Here the $\phi_d = \nu_{det}\tau_f$ and FIDs measured with the detuning frequency $\nu_{det} = 40 \text{ MHz}$. Figure. 11 (b) shows the signals recorded for the both V_{Si}^- as a function of dephasing time delay τ_f . The experimental recorded signal of V_2 (V_3) vacancy fitted to the

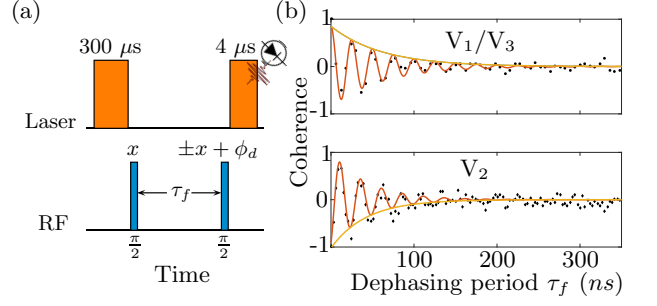


FIG. 11. (a) Pulse sequence to measure the FID of V_{Si}^- . (b) The experimental recorded FID signal of V_{Si}^- at room temperature.

function

$$S_{x+\phi_d} - S_{-x+\phi_d} = A \cos(2\pi\nu_{det}\tau_f + c) e^{-\tau_f/T_2^*}, \quad (7)$$

where $S_{\pm x+\phi_d}$ is the average PL signal measured with $\pi/2$ RF detection pulse of phase $\pm x + \phi_d$. After fitting the experimental signal in the Eq.7, the $T_2^* = 42 \text{ ns}$ ($65 \pm 5 \text{ ns}$).

Figure 12(a) shows the pulse sequence for measuring the spin coherence time under the CPMG sequence. We first polarized the spin ensemble with the $300 \mu\text{s}$ laser pulse, and then the coherence was created with the $\pi/2$ pulse. The CPMG sequence was applied i.e., a train of $2N$ π pulses applied along the y -axis, which was separated by the delay $\tau_c/2$ from each other. At last coherence was converted into the population with the application of second $\pi/2$ pulse along the x -axis and PL signal was measured with the second laser pulse. The experiment was repeated for recording the reference signal for which the pulse sequence was same except the second $\pi/2$ pulse was applied along the $-x$ -axis. The difference between the experimentally measured PL signals was fitted to the function

$$S_x - S_{-x} = A e^{-(\tau_{CPMG}/T_2^{CPMG})^n}, \quad (8)$$

where the time period $\tau_{CPMG} = 2N(\tau_c + \pi \text{ pulse duration})$, $2N$ is number of π pulses.

APPENDIX E: PL POLARIZATION

Figure 13 shows the polarization plots of the V_1 , V_2 and V_3 ZPL intensities recorded perpendicular and parallel to the c -axis at 5K. A polarizer was used for selecting the particular PL polarization. Before detecting the signal, individual ZPLs of the different silicon vacancies were selected using the monochromator or suitable bandpass filters. With the monochromator, we can select a very narrow bandwidth and minimise the contribution from the

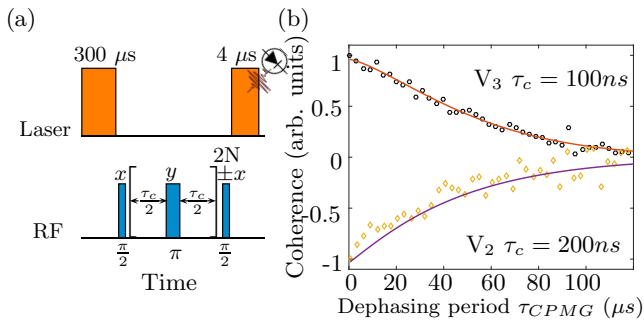


FIG. 12. (a) Pulse sequence for measuring the spin coherence time under the CPMG sequence. (b) The experimental recorded decay of the spin coherence of V_{Si}^- during the CPMG sequence at room temperature.

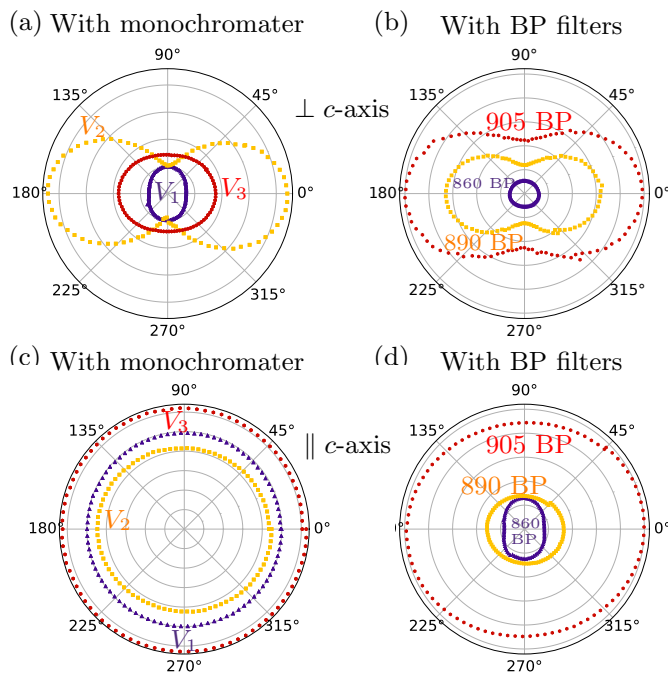


FIG. 13. Polarization plots of the ZPL intensities for the different centers at 5 K, (a) with monochromator, and (b) with bandpass filters for emission perpendicular to the c -axis ; (c) with monochromator, and (d) with bandpass filters, for emission parallel to the c -axis. θ is the angle difference between the initial and final position of the polarizer's transmission axis and in case of $\perp c$ -axis orientation, 0° is \parallel to c -axis.

phonon sidebands of the other vacancies. With the optical bandpass filters, the width of the passband is larger (10 nm), but it has the advantage of passing more signal, which is important for the ODMR measurements. Figure 13 (a) shows the data for PL emission perpendicular to the c -axis using the monochromator. The emission of V_2 is linearly polarized perpendicular to the c -axis, while that of V_1 is almost unpolarized [13]. In the case of V_3 , a significant signal contribution comes from the phonon side band (PSB) of V_1 and V_2 . The data in

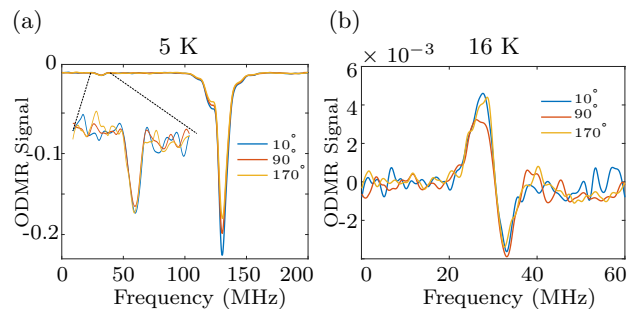


FIG. 14. (a) Plot of ODMR recorded for different polarizations at 5 K. (b) ODMR of V_1/V_3 for different polarizations at 16 K. In both cases, PL was emitted \parallel to the c -axis. $\theta = 0$ corresponds to vertical polarization.

figure 13 (b) were recorded with different bandpass filters; accordingly, they contain larger contributions from PSB other centers, which results in lower polarization. In contrast to previous work [13] we did not apply a background correction, since the available data do not allow a reliable separation into contributions from the different ZPLs and sidebands.

APPENDIX F: ODMR POLARIZATION

Since we were not able to separate the ODMR signal of V_1 in PL emission $\perp c$ -axis we recorded ODMR spectra for different orientations of the polarization for the PL emitted $\parallel c$ -axis. Figure 14 (a) shows several ODMR spectra recorded at 5 K for different orientations of a polarizer in the detection path. The amplitude of the signal near 28 MHz does not change significantly, but the signal near 130 MHz varies by $\approx 21\%$. Figure 14 (b) shows the ODMR spectrum measured at 16 K from 0 to 60 MHz. At this temperature, the signal appears to consist of a positive and a negative contribution. The amplitude of the positive peak varies with the polarization by $\approx 31\%$ while the negative peak remains constant. This appears to be consistent with the different polarization dependence of V_1 and V_3 discussed in Appendix E.

ACKNOWLEDGMENTS

This work was supported by the Deutsche Forschungsgemeinschaft in the frame of the ICRC TRR 160 (Project No. C7) and by RFBR, project number 19-52-12058.

NOTE

All experiments were done on the sample provided by A. N. A. and P. G. B well before the EU sanctions. H.S and D.S did experimental measurements and data analysis.

To our knowledge, these results do not have any short-term economic or military relevance.

-
- [1] J. Wang, Y. Zhou, X. Zhang, F. Liu, Y. Li, K. Li, Z. Liu, G. Wang, and W. Gao, Efficient generation of an array of single silicon-vacancy defects in silicon carbide, *Phys. Rev. Applied* **7**, 064021 (2017).
- [2] J. Rabkowski, D. Pefitsis, and H. Nee, Silicon carbide power transistors: A new era in power electronics is initiated, *IEEE Industrial Electronics Magazine* **6**, 17 (2012).
- [3] V. Izhevskiy, L. Genova, J. Bressiani, and A. Bressiani, Review article: silicon carbide, Structure, properties and processing. *Cerâmica* **46**, 4 (2000).
- [4] N. Gonzalez Szwacki, Structural and electronic properties of silicon carbide polytypes as predicted by exact exchange calculations, *Computational Condensed Matter* **13**, 55 (2017).
- [5] S. A. Tarasenko, A. V. Poshakinskiy, D. Simin, V. A. Soltamov, E. N. Mokhov, P. G. Baranov, V. Dyakonov, and G. V. Astakhov, Spin and optical properties of silicon vacancies in silicon carbide - a review (phys. status solidi b 1/2018), *physica status solidi (b)* **255**, 1870101 (2018).
- [6] S. P. Pavunny, A. L. Yeats, H. B. Banks, E. Bielejec, R. L. Myers-Ward, M. T. DeJarld, A. S. Bracker, D. K. Gaskill, and S. G. Carter, Arrays of si vacancies in 4h-sic produced by focused li ion beam implantation, *Scientific reports* **11**, 3561 (2021).
- [7] D. Riedel, F. Fuchs, H. Kraus, S. Väh, A. Sperlich, V. Dyakonov, A. A. Soltamova, P. G. Baranov, V. A. Ilyin, and G. V. Astakhov, Resonant addressing and manipulation of silicon vacancy qubits in silicon carbide, *Physical review letters* **109**, 226402 (2012).
- [8] P. G. Baranov, A. P. Bundakova, A. A. Soltamova, S. B. Orlinskii, I. V. Borovykh, R. Zondervan, R. Verberk, and J. Schmidt, Silicon vacancy in sic as a promising quantum system for single-defect and single-photon spectroscopy, *Phys. Rev. B* **83**, 125203 (2011).
- [9] V. Ivády, J. Davidsson, N. T. Son, T. Ohshima, I. A. Abrikosov, and A. Gali, Identification of si-vacancy related room-temperature qubits in 4h silicon carbide, *Phys. Rev. B* **96**, 161114 (2017).
- [10] E. Sörman, N. T. Son, W. M. Chen, O. Kordina, C. Hallin, and E. Janzén, Silicon vacancy related defect in 4h and 6h sic, *Phys. Rev. B* **61**, 2613 (2000).
- [11] T. Biktagirov, W. G. Schmidt, U. Gerstmann, B. Yavkin, S. Orlinskii, P. Baranov, V. Dyakonov, and V. Soltamov, Polytypism driven zero-field splitting of silicon vacancies in 6h-sic, *Phys. Rev. B* **98**, 195204 (2018).
- [12] J. Davidsson, V. Ivády, R. Armiento, T. Ohshima, N. T. Son, A. Gali, and I. A. Abrikosov, Identification of divacancy and silicon vacancy qubits in 6h-sic, *Applied Physics Letters* **114**, 112107 (2019), <https://doi.org/10.1063/1.5083031>.
- [13] I. Breev, Z. Shang, A. Poshakinskiy, H. Singh, Y. Berencén, M. Hollenbach, S. Nagalyuk, E. Mokhov, R. Babunts, P. Baranov, *et al.*, Inverted fine structure of a 6h-sic qubit enabling robust spin-photon interface, *npj Quantum Information* **8**, 1 (2022).
- [14] T. C. Hain, F. Fuchs, V. A. Soltamov, P. G. Baranov, G. V. Astakhov, T. Hertel, and V. Dyakonov, Excitation and recombination dynamics of vacancy-related spin centers in silicon carbide, *Journal of Applied Physics* **115**, 133508 (2014), <https://doi.org/10.1063/1.4870456>.
- [15] F. Fuchs, B. Stender, M. Trupke, D. Simin, J. Pflaum, V. Dyakonov, and G. Astakhov, Engineering near-infrared single-photon emitters with optically active spins in ultrapure silicon carbide, *Nature communications* **6**, 1 (2015).
- [16] C. A. Kasper, *Engineering of Highly Coherent Silicon Vacancy Defects in Silicon Carbide*, Ph.D. thesis, Universität Würzburg (2021).
- [17] H. Singh, M. A. Hollberg, A. N. Anisimov, P. G. Baranov, and D. Suter, Multi-photon multi-quantum transitions in the spin- $\frac{3}{2}$ silicon-vacancy centers of sic, *Phys. Rev. Research* **4**, 023022 (2022).
- [18] J.-Y. Zhou, Q. Li, Z.-Y. Hao, F.-F. Yan, M. Yang, J.-F. Wang, W.-X. Lin, Z.-H. Liu, W. Liu, H. Li, *et al.*, Experimental determination of the dipole orientation of single color centers in silicon carbide, *ACS Photonics* **8**, 2384 (2021).
- [19] E. Janzén, A. Gali, P. Carlsson, A. Gällström, B. Magnusson, and N. T. Son, The silicon vacancy in sic, *Physica B: Condensed Matter* **404**, 4354 (2009).
- [20] H. Singh, A. N. Anisimov, S. S. Nagalyuk, E. N. Mokhov, P. G. Baranov, and D. Suter, Experimental characterization of spin-3/2 silicon vacancy centers in 6h-sic, *Phys. Rev. B* **101**, 134110 (2020).
- [21] V. A. Soltamov, C. Kasper, A. V. Poshakinskiy, A. N. Anisimov, E. N. Mokhov, A. Sperlich, S. A. Tarasenko, P. G. Baranov, G. V. Astakhov, and V. Dyakonov, Excitation and coherent control of spin qubit modes in silicon carbide at room temperature, *Nature Communications* **10**, 1678 (2019).
- [22] H. Singh, A. N. Anisimov, I. D. Breev, P. G. Baranov, and D. Suter, Optical spin initialization of spin- $\frac{3}{2}$ silicon vacancy centers in 6h-SiC at room temperature, *Phys. Rev. B* **103**, 104103 (2021).
- [23] G. Astakhov, D. Simin, V. Dyakonov, B. Yavkin, S. Orlinskii, I. Proskuryakov, A. Anisimov, V. Soltamov, and P. Baranov, Spin centres in sic for quantum technologies, *Applied Magnetic Resonance* **47**, 793 (2016).
- [24] D. Suter, Optical detection of magnetic resonance, *Magnetic Resonance* **1**, 115 (2020).
- [25] D. Carbonera, Optically detected magnetic resonance (odmr) of photoexcited triplet states, *Photosynthesis research* **102**, 403 (2009).
- [26] A. Abragam, *The principles of nuclear magnetism* (Oxford University Press, UK, 1961).
- [27] N. F. Ramsey, A molecular beam resonance method with separated oscillating fields, *Phys. Rev.* **78**, 695 (1950).
- [28] E. L. Hahn, Spin echoes, *Phys. Rev.* **80**, 580 (1950).
- [29] D. Simin, H. Kraus, A. Sperlich, T. Ohshima, G. V. Astakhov, and V. Dyakonov, Locking of electron spin coherence above 20 ms in natural silicon carbide, *Phys. Rev. B* **95**, 161201(R) (2017).